



## Surface reconstruction enabling MoO<sub>2</sub>/MoP hybrid for efficient electrocatalytic oxidation of *p*-xylene to terephthalic acid

Ye Lv <sup>a</sup>, Mao Peng <sup>a,b</sup>, Weiwei Yang <sup>a</sup>, Menghui Liu <sup>a</sup>, Aiqun Kong <sup>c</sup>, Yan Fu <sup>a,\*</sup>, Wei Li <sup>a</sup>, Jinli Zhang <sup>a,c, \*\*</sup>

<sup>a</sup> School of Chemical Engineering and Technology, Tianjin University, Tianjin 300350, China

<sup>b</sup> Institute of Shaoxing, Tianjin University, Zhejiang 312300, China

<sup>c</sup> School of Chemistry and Chemical Engineering/State Key Laboratory Incubation Base for Green Processing of Chemical Engineering, Shihezi University, Shihezi 832003, China



### ARTICLE INFO

#### Keywords:

Electrocatalytic oxidation  
*p*-Xylene  
Transition metal phosphide  
Surface reconstruction  
Terephthalic acid

### ABSTRACT

Selective oxidation of *p*-xylene (PX) to terephthalic acid (TA) remains exceptionally challenging since it easily undergoes deep oxidation. Herein, a nickel foam-supported molybdenum dioxide/molybdenum phosphide hybrid electrocatalyst (MoO<sub>2</sub>/MoP/NF) is reported for highly selective generation of TA via electrocatalytic oxidation (ECO) of PX in alkaline medium. The efficient MoO<sub>2</sub>/MoP/NF anode material displays a unique cluster-like nanocone architecture, showing abundant active sites and rapid charge transfer kinetics. Benefit from the synergy between MoO<sub>2</sub> and MoP, the MoO<sub>2</sub>/MoP/NF provides a high TA selectivity of 94.8% and an outstanding faradaic efficiency of 76.9% at the conversion of 71.6%. Additionally, the anodic oxidation of PX over MoO<sub>2</sub>/MoP/NF promotes the cathodic hydrogen production. The potential-induced surface reconstruction of the as-synthesized MoO<sub>2</sub>/MoP/NF yields new phases of phosphomolybdate and potassium molybdate. The top P site on the phosphomolybdate surface facilitates the adsorption of reaction intermediates but weakens the adsorption of TA, thereby yielding high selectivity toward TA.

### 1. Introduction

As the shortage of traditional energy and environmental pollution have become the major problems restricting economic and social development, it is very urgent to find pollution-free resources. Hydrogen is considered to be the most promising energy carrier to replace fossil fuels in the future due to its high energy density, abundant sources and sustainability [1]. Hydrogen production by water electrolysis based on renewable energies can not only obtain high purity products, but also reduce carbon emissions, which is in line with the strategy of sustainable [2,3]. However, anodic oxygen evolution reaction (OER) is a four-electron process with slow kinetics that leads to the actual voltage of water electrolysis much higher than the theoretical voltage (1.23 V), which has become a bottleneck limiting the development of hydrogen production by water electrolysis [4–7]. Up to now, replacing OER with a thermodynamically favorable electrocatalytic oxidation (ECO) of organics including alcohols [8,9], urea [10,11], hydrazine [12,13] and 5-hydroxymethyl furfural [14,15] not only reduces the anodic

overpotential, but also produces high value-added chemicals coupled with hydrogen production [16–18]. The expansion of new ECO systems coupled with hydrogen production for green synthesis of economically valuable organic compounds becomes a hot issue.

As an important chemical intermediate, terephthalic acid (TA) is usually obtained in industry through aerobic oxidation of *p*-xylene (PX) using Co-Mn-Br as the catalyst at 200 °C and 3.0 MPa in acetic acid [19]. Although the conversion of PX and the selectivity of TA are up to 90%, bromine corrodes equipment at high temperature and produces harmful by-products, resulting in high production costs and environmental pollution. Zhang et al. [20] developed an “out-slot type” indirect electrochemical method for the synthesis of TA using Cr<sub>2</sub>O<sub>7</sub><sup>2-</sup>/Cr<sup>3+</sup> as the redox pair in 5 M H<sub>2</sub>SO<sub>4</sub> at 110 °C, giving the maximum TA yield of 78.5%. Such indirect electrochemical method involves concentrated acidic electrolyte, high reaction temperature and toxic catalyst, which lead to high equipment cost and environmental pollution. Raj et al. [21] performed the ECO of PX in an undivided electrolytic cell with an emulsion consists of CHCl<sub>3</sub> and 0.46 M H<sub>2</sub>SO<sub>4</sub> containing 2% NaNO<sub>3</sub>

\* Corresponding author.

\*\* Corresponding author at: School of Chemical Engineering and Technology, Tianjin University, Tianjin 300350, China.

E-mail addresses: [fuyan@tju.edu.cn](mailto:fuyan@tju.edu.cn) (Y. Fu), [zhangjinli@tju.edu.cn](mailto:zhangjinli@tju.edu.cn) (J. Zhang).

( $V_{\text{CHCl}_3}/V_{\text{H}_2\text{SO}_4} = 1/2$ ). Under the optimal experimental conditions, an 84% selectivity of *p*-tolualdehyde was obtained at the PX conversion of 88%. Up to now, most electrocatalytic methods on the synthesis of aromatic acids adopted aromatic alcohols as raw materials [9,22,23]. The selective electrocatalytic oxidation of  $-\text{CH}_3$  to  $-\text{COOH}$  has not been reported. In the oxidation of PX, high dissociation energy is required for the activation of inert C-H bond. The  $-\text{COOH}$  group of TA is much easier to be oxidized with respect to the C-H bond of PX. Hence, it is still challenging to achieve high selectivity of TA owing to seriously deep oxidation [24]. Design of suitable electrocatalysts is highly desirable to realize the economically electrochemical method for TA production.

Transition metal phosphides have been widely employed in electrocatalysis due to their earth-abundance, remarkable catalytic activity and electrical conductivity [25–27]. Recent studies have established that surface reconstitution of transition metal phosphide-based precatalysts plays a decisive role on the catalytic performance via potential-induced evolution of crystalline phase structure, morphology as well as electronic valence state [28–30]. Qiu et al. [31] reported the reconstruction of Co-Fe phosphide precatalysts into amorphous Co-Fe hydroxide nanosheets under anodic potential. The etching effect caused by the leached phosphorus species promoted the oxidation of residual Co-Fe species for deeply bulk reconstitution. The amorphous Co-Fe catalysts with highly exposed active sites showed excellent OER activities (254 mV at 10 mA cm $^{-2}$  and 292 mV at 100 mA cm $^{-2}$ ) and durability (15 days at 100 mA cm $^{-2}$ ). Tao et al. [32] prepared cactus-like NiCoP nanosheets for ECO of HMF to FDCA. The Co substitution could adjust the valence state of Ni, making the surface reconstruction of NiCoP to NiOOH more easily. The selectivity of FDCA was up to 99.6% at the conversion of 99.8%, giving the faradaic efficiency of 96.1%. Nevertheless, most studies focus on the transformation process of metal

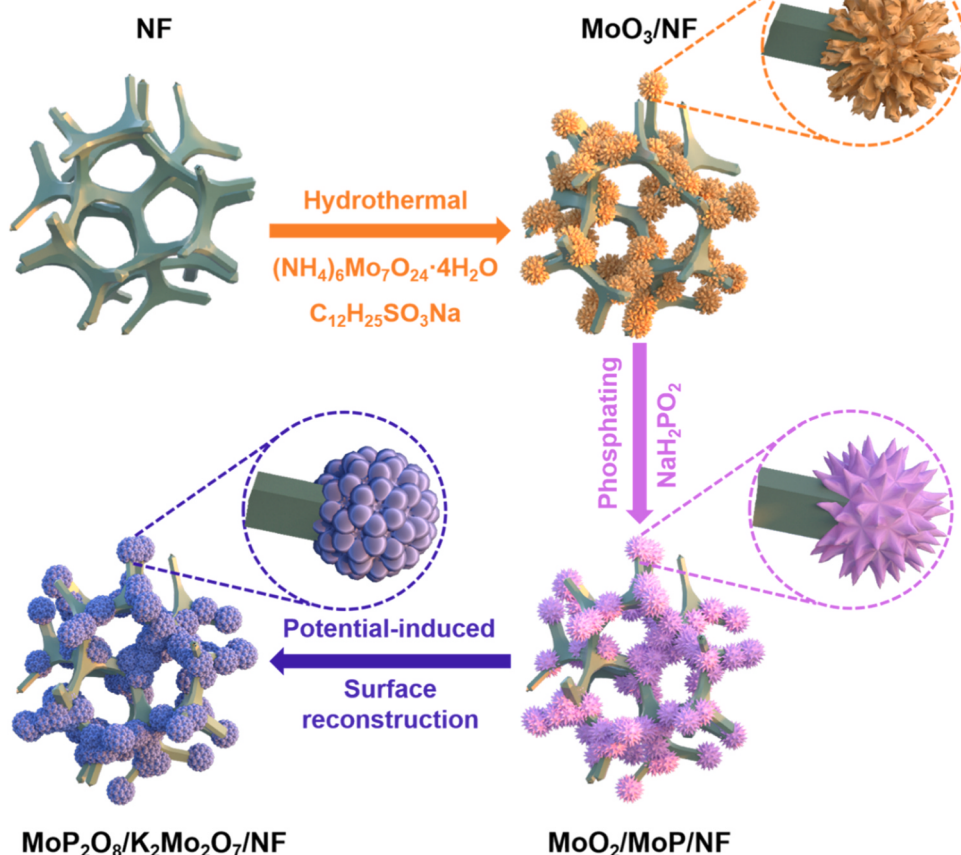
during surface reconstruction and subsequent oxidation reaction. The vital role of P remains elusive now.

In this work, we fabricated a nickel foam-supported hybrid precatalyst  $\text{MoO}_2/\text{MoP}/\text{NF}$  by a facile two-step hydrothermal-phosphorylation method for selective oxidation of PX coupled with hydrogen production. The unique morphology endows the  $\text{MoO}_2/\text{MoP}$  electrocatalyst with large surface area and highly exposed active sites. The surface reconstruction of  $\text{MoO}_2/\text{MoP}$  into  $\text{MoP}_2\text{O}_8/\text{K}_2\text{Mo}_2\text{O}_7$  facilitates moderate adsorption with intermediates but weak adsorption with TA, thereby yielding high selectivity toward TA. The  $\text{MoO}_2/\text{MoP}/\text{NF}$  anode material not only manifests outstanding selectivity for TA, but also promotes the hydrogen production through coupling the cathodic hydrogen evolution with anodic PX oxidation. This work paves a promising pathway to achieve efficient ECO process via adjusting the dynamic active center based on potential-driven surface reconstitution of transition metal phosphide.

## 2. Experimental

### 2.1. Preparation of $\text{MoO}_2/\text{MoP}/\text{NF}$ electrodes

The  $\text{MoO}_2/\text{MoP}/\text{NF}$  electrodes were prepared via a hydrothermal reaction followed by a phosphorylation process depicted in Scheme 1. Firstly, a piece of nickel foam (NF,  $1.5 \times 3 \text{ cm}^2$ ) was soaked with 3 M hydrochloric acid for 15 min and then washed with deionized water and ethanol to remove surface impurities. Subsequently, 20 mM  $(\text{NH}_4)_6\text{Mo}_7\text{O}_{24} \cdot 4\text{H}_2\text{O}$  and 100 mM  $\text{C}_{12}\text{H}_{25}\text{SO}_3\text{Na}$  were added to 20 mL deionized water. After vigorously stirring for 30 min, the treated NF was put into the above solution. Then, the mixture was transferred to a 50 mL teflon-lined reactor and treated at different hydrothermal



**Scheme 1.** Schematic illustration for the synthesis procedure and morphological evolution of  $\text{MoO}_2/\text{MoP}/\text{NF}$ .

temperature for 12 h. After the reactor was cooled to room temperature, NF was washed with ethanol and deionized water, and subsequently dried at 80 °C for 12 h to obtain MoO<sub>3</sub>/NF-x (x represents the hydrothermal temperature; x = 100 °C, 120 °C, 140 °C, 160 °C, respectively). Finally, the MoO<sub>2</sub>/MoP/NF-x electrodes were obtained by calcining MoO<sub>3</sub>/NF-x at 600 °C for 2 h under argon atmosphere with 2.5 g Na<sub>2</sub>PO<sub>2</sub>.

The MoO<sub>2</sub>/NF electrodes and MoP/NF electrodes were also prepared as controls. The experimental details were described in the [supplementary information](#).

## 2.2. Electrochemical measurements

The electrochemical measurements were depicted in the [supplementary information](#).

## 2.3. Electrocatalytic oxidation of *p*-xylene

ECO of PX was conducted on a IT7620 DC power supply using an H-type electrochemical cell. The anodic electrolyte contained 25 mM PX dissolved in 1 M KOH solution (V<sub>H2O</sub>/V<sub>CH3CN</sub> = 7/3). The cathodic electrolyte was 1 M KOH aqueous solution. The area of MoO<sub>2</sub>/MoP/NF submerged in the electrolyte was set as 1 × 3 cm<sup>2</sup>. PX was quantitatively analyzed by gas chromatography (GC, Shimadzu). The oxidized products were detected by high performance liquid chromatography-mass spectrometry (HPLC-MS, Agilent). Further product analysis conditions were provided in the [supplementary information](#). The conversion (%), selectivity (%) and faradaic efficiency (%) were calculated as follows:

$$\text{Conversion (\%)} = \frac{\text{moles of PX consumed}}{\text{moles of initial PX}} \times 100\%$$

$$\text{Selectivity (\%)} = \frac{\text{moles of product}}{\text{moles of PX consumed}} \times 100\%$$

$$\text{Faradaic efficiency (\%)} = \frac{e \cdot n \cdot F}{Q} \times 100\%$$

where *e* is the number of electrons transferred during the oxidation of PX to TA (*e* = 12), *n* is the mole of TA produced, *F* is the Faraday constant (96,500 C/mol) and *Q* is the total electrons passed. The moles of substances were calculated from the concentration obtained by the standard curve ([Figs. S1–S5](#)).

## 2.4. Physicochemical characterizations

The details of physicochemical characterizations were presented in the [supplementary information](#).

## 2.5. Density functional theory (DFT) calculations

The details of DFT calculations were provided in the [supplementary information](#).

## 3. Results and discussion

### 3.1. Hybrid MoO<sub>2</sub>/MoP/NF with cluster-like nanocone structure via hydrothermal- phosphorylation process

The MoO<sub>2</sub>/MoP/NF-x precatalysts were prepared by a hydrothermal treatment followed by a phosphorylation process ([Scheme 1](#)). After the hydrothermal treatment at 100 °C, the XRD peaks match well with monoclinic MoO<sub>3</sub>·2 H<sub>2</sub>O (PDF#16-0497) ([Fig. S6](#)) [33]. With the increase of hydrothermal temperature, the hexagonal MoO<sub>3</sub> (PDF#21-0569) [34] becomes distinguishable. All the samples obtained at high hydrothermal temperature (above 120 °C) exhibit two distinct crystalline phases with good crystallinity including hexagonal MoO<sub>3</sub> and monoclinic MoO<sub>3</sub>·2 H<sub>2</sub>O. Moreover, the average crystallite sizes evaluated by Scherrer's equation progressively increase with increasing the hydrothermal temperatures ([Table S1](#)). Raman spectra ([Fig. S7](#)) of all the samples exhibit four characteristic peaks at 285, 339, 810 and 992 cm<sup>-1</sup>, respectively. The peaks at 285 and 339 cm<sup>-1</sup> belong to the

O=M=O wagging (B<sub>2g</sub> vibrational mode) and O-M-O bending (A<sub>g</sub> vibrational mode) of MoO<sub>3</sub>, while the peaks at 810 and 992 cm<sup>-1</sup> are attributable to the M=O stretching (A<sub>g</sub> vibrational mode) of MoO<sub>3</sub> [35, 36]. So, it is demonstrated the formation of MoO<sub>3</sub> after hydrothermal treatment.

The temperature-dependent crystalline phases and structural features of MoO<sub>2</sub>/MoP/NF-x were also disclosed by XRD and Raman spectra. After phosphorylation, the MoO<sub>2</sub>/MoP/NF-100 shows a dominant crystalline phase of monoclinic MoO<sub>2</sub> (PDF#32-0671) [37–39] with trace hexagonal MoP (PDF#24-0771) [40] ([Fig. 1a](#)). As the hydrothermal temperature continues to increase, the hexagonal MoP becomes more pronounced. Notably, the as-prepared samples display both monoclinic MoO<sub>2</sub> and hexagonal MoP phases with good crystallinity at high hydrothermal temperature (above 120 °C). After the phosphorylation process, the as-obtained MoO<sub>2</sub>/MoP/NF exhibits smaller crystallite size relative to the corresponding MoO<sub>3</sub>/NF ([Table S2](#)), which might be attributed to the changes of crystalline phases during the phosphorylation process [41,42]. Similar changes were also found in Raman spectra ([Fig. 1b](#)). The characteristic bands located at 401 and 743 cm<sup>-1</sup> are consistent with the features of MoP and the Mo-O stretching vibration of MoO<sub>2</sub> [43,44]. Accordingly, it can be deduced that MoO<sub>3</sub> converts to MoO<sub>2</sub> and MoP in the presence of PH<sub>3</sub> and H<sub>2</sub> generated from Na<sub>2</sub>PO<sub>2</sub> decomposition [45].

The chemical valence states for the samples after hydrothermal and phosphorylation were analyzed by XPS. After hydrothermal reaction ([Fig. S8](#)), the B.E.s of Mo 3d at 235.47 and 232.31 eV are responsible for the Mo (VI) oxidation state of MoO<sub>3</sub> [46]. The high-resolution XPS spectra for O 1s show two peaks at 530.34 and 532.25 eV respectively, which can be derived from Mo (VI)-O of MoO<sub>3</sub> and OH<sub>2</sub>O (adsorbed water) [47]. After phosphorylation ([Figs. 1c–e, S9–S11](#)), the high-resolution XPS spectra of Mo 3d can be fitted into five peaks. The peaks at 228.29, 229.63 and 232.25 eV correspond well to Mo<sup>δ+</sup> species of MoP, Mo (IV) and Mo (VI) species respectively, indicating the coexistence of MoP and MoO<sub>2</sub> with partially oxidized surface [48,49]. The high-resolution O1s spectra exhibit three peaks at 531.08, 532.57 and 533.31 eV, which originate from the Mo(IV)-O bond from MoO<sub>2</sub>, P-O and P = O bonds [48]. The B.E. of P 2p at 129.72, 130.70 and 133.89 eV can be assigned to P<sup>δ-</sup> of MoP and P-O or PO<sub>4</sub><sup>3-</sup>, respectively [44]. It is evident that MoO<sub>3</sub> transforms into hybrid MoO<sub>2</sub>/MoP during the phosphorylation process. As compared to other samples ([Table S3](#)), XPS analysis demonstrates that MoO<sub>2</sub>/MoP/NF-140 has the lowest MoO<sub>2</sub>/MoP surface ratio (3.1:1), which means that MoO<sub>2</sub>/MoP/NF-140 has the highest proportion MoP.

The morphologies and structural features of as-prepared samples were characterized using SEM and TEM. Initially, MoO<sub>3</sub> nanorods with cone-like structures and rough surfaces were sparsely grown on the surface of NF skeleton at 100 °C ([Figs. S12, S13a–b](#)). As the hydrothermal temperature increases to 120 °C, nanocones aggregate into large clusters ([Fig. S13c–d](#)). At 140 °C, nanocone clusters become more densely and homogeneously distribute on the NF surface ([Fig. S13e–f](#)). However, with the hydrothermal temperature up to 160 °C, the stacked nanosheet-like structures can be observed in addition to nanocone clusters ([Fig. S13g–h](#)). After phosphorylation at 140 °C ([Figs. 2a–b, S14](#)), the three-dimensional architecture of cluster-like nanocone maintains whereas the rough surface becomes smooth. Such cluster-like nanocone architecture can expose abundant active sites that are easily contacted by reactants.

The MoO<sub>3</sub>/NF-140 displays the lattice spacing of 0.315 and 0.191 nm respectively as revealed by HRTEM, which are indexed to the (334) plane of MoO<sub>3</sub> and the (404) plane of MoO<sub>3</sub>·2H<sub>2</sub>O. The specific features of the sample with the (334) plane of MoO<sub>3</sub>, the (424) plane and (404) plane of MoO<sub>3</sub>·2H<sub>2</sub>O are revealed by the SAED pattern ([Fig. S15](#)). For the MoO<sub>2</sub>/MoP/NF-140, the lattice spacing of 0.206 and 0.239 nm can be precisely assigned to the (–211) planes of MoO<sub>2</sub> and the (101) plane of MoP ([Fig. 2c–e](#)) [38,40]. The SAED pattern further verifies that the sample is composed of crystalline MoO<sub>2</sub> and MoP ([Fig. 2f](#)). The

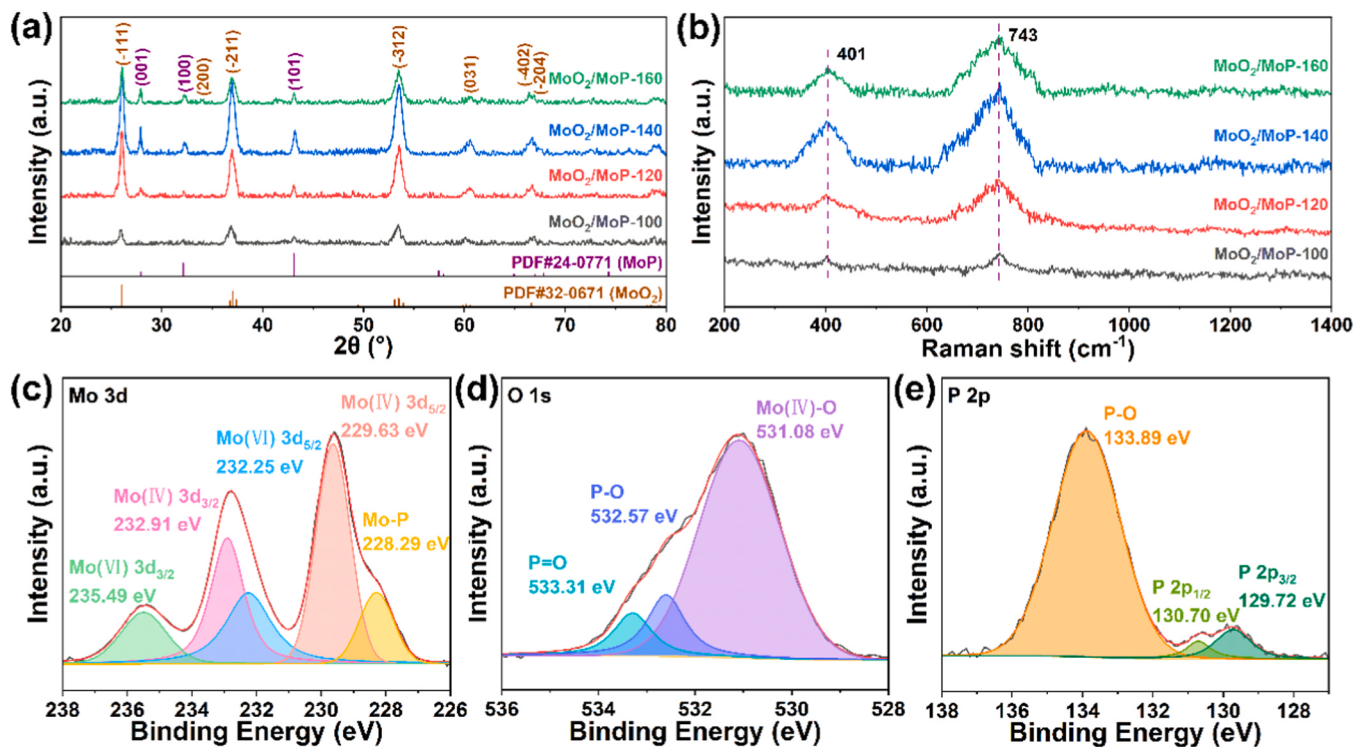


Fig. 1. (a) XRD patterns and (b) Raman spectra of as-prepared samples (the samples were scraped from NF for the XRD and Raman measurements). High-resolution XPS spectra for MoO<sub>2</sub>/MoP/NF-140. (c) Mo 3d, (d) O 1s, (e) P 2p.

corresponding elemental mapping verify that Mo, O and P uniformly distribute on the MoO<sub>2</sub>/MoP/NF-140 (Fig. 2g-j). So, it is demonstrated that MoO<sub>2</sub>/MoP/NF electrode materials with large surface areas and highly exposed active sites can be obtained via a simple hydrothermal-phosphorylation method.

As a control, the structure and morphology of the MoO<sub>2</sub>/NF-140 were also investigated. The MoO<sub>2</sub>/NF-140 obtained by a hydrothermal-calcining procedure shows a typical crystalline phase of monoclinic MoO<sub>2</sub> (PDF#32-0671) (Fig. S16). It can be seen that small rectangular nanoparticles aggregate to form large clusters (Fig. S17). The lattice spacing of MoO<sub>2</sub>/NF-140 (0.205 nm) matches well with the (111) plane of MoO<sub>2</sub>. In addition, the corresponding elemental mapping shows the uniform distribution of Mo and O in MoO<sub>2</sub>/NF-140 (Fig. S18).

### 3.2. Electrocatalytic oxidation of PX with high selectivity of TA

The ECO of PX utilizing MoO<sub>2</sub>/MoP/NF electrodes under different conditions were presented in Fig. 3 and Table S4. The MoO<sub>2</sub>/MoP/NF exhibits considerably higher TA selectivity (94.8%) as compared to other catalysts including NF (4.4%), commercial MoP/NF (5.8%) and MoO<sub>2</sub>/NF (40.0%), implying a synergistic effect of MoO<sub>2</sub> and MoP in the ECO process of PX (Fig. 3a). Regarding the hydrothermal temperature adopted for MoO<sub>2</sub>/MoP/NF, the conversion of PX shows no obvious difference. However, the selectivity of TA is highly dependent upon the hydrothermal temperature, and reaches to the highest value at 140 °C, followed by an apparent decrease at 160 °C (Fig. 3b). As a result, the MoO<sub>2</sub>/MoP/NF-140 possesses the optimal TA selectivity of 94.8% at the PX conversion of 71.6%. HPLC-MS (Fig. S19, S20) analysis unveils the reaction pathway of ECO of PX, which involves a series of oxidation intermediates of *p*-tolualdehyde (*p*-TALD), *p*-toluic acid (*p*-TA), 4-carboxybenzaldehyde (4-CBA) and terephthalic acid (TA) (Fig. 3c). *p*-TALD, *p*-TA and 4-CBA are the major products within the initial 2 h, which shows descending *p*-TALD and ascending *p*-TA and 4-CBA. TA occurs at 3 h and becomes the dominant product after 4 h. Its selectivity progressively grows within 3–6 h. Accordingly, the reaction pathway for

ECO of PX over MoO<sub>2</sub>/MoP/NF-140 was provided in Fig. 3d.

With the applied potentials stepping from 1.4 to 1.6 V vs RHE, both the conversion of PX and the selectivity of TA gradually ascends, accompanied by the decreased selectivity for *p*-TA and 4-CBA. The ECO of PX achieves the highest TA selectivity of 93.5% at 1.6 V vs RHE, giving the PX conversion of 73.8% (Fig. 3e).

Moreover, operating current density was also optimized (Fig. 3f). The ECO of PX exhibits the best performance at 10 mA cm<sup>-2</sup> since it undergoes apparent over-oxidation at high current density. The faradaic efficiency reaches up to an outstanding 76.9% under the optimal conditions (Fig. S21). As summarized in Table S5, it can be clearly seen that the MoO<sub>2</sub>/MoP/NF electrode material achieves superior TA selectivity to other electrocatalysts and most of the reported catalysts in thermo-catalysis and photocatalysis.

The cathodic hydrogen production was measured via a drainage method under ECO and OER conditions respectively [50] (Figs. 3g, S22). The hydrogen amount coupling with ECO of PX (13.5–14 mL/h) is higher than that under OER condition (9–10 mL/h), which indicates that the MoO<sub>2</sub>/MoP/NF-140 could promote the hydrogen production by replacing OER with ECO.

The superiority of ECO to OER was further corroborated by electrochemical measurements. LSV profiles (Fig. 4a-b) demonstrate that the MoO<sub>2</sub>/MoP/NF-140 exhibits obviously lower overpotential at 10 mA cm<sup>-2</sup> with PX (123 mV) than that without PX (148 mV). This difference becomes more significant at high current density, which proves that the MoO<sub>2</sub>/MoP/NF-140 is preferential to drive ECO of PX rather than OER. Particularly, the MoO<sub>2</sub>/MoP/NF-140 affords a considerably smaller Tafel slope of 39.8 mV dec<sup>-1</sup> with PX added relative to OER (60.8 mV dec<sup>-1</sup>), which is indicative of a favorable reaction kinetics for the ECO of PX. Furthermore, a two-electrode hybrid water electrolysis system using MoO<sub>2</sub>/MoP/NF-140 as the anode and Pt/C as the cathode were constructed to test the overall performance. LSV curves display that the PX electro-oxidation assisted water electrolysis (87 mV at 10 mA cm<sup>-2</sup>) exhibits lower overpotential than traditional water electrolysis (101 mV at 10 mA cm<sup>-2</sup>) at the same current density

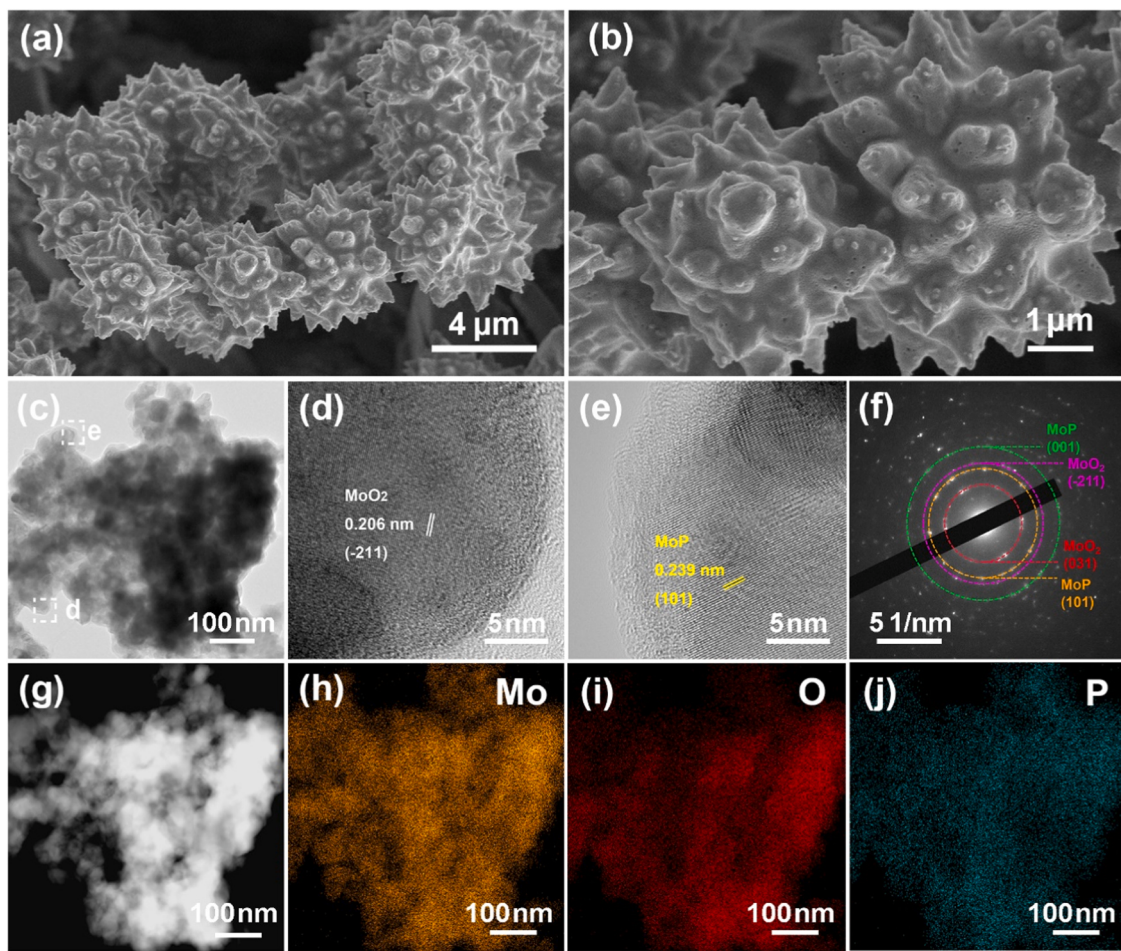


Fig. 2. (a, b) SEM images; (c) TEM image, (d, e) HRTEM images, (f) SAED pattern and (g-j) the corresponding TEM elemental mapping of  $\text{MoO}_2/\text{MoP}/\text{NF-140}$ .

(Fig. S23a). Significantly, PX electro-oxidation assisted water electrolysis requires only 1.42 V to drive  $10 \text{ mA cm}^{-2}$  and possesses a superior stability with a negligible deactivation over 40 h (Fig. S23b). Comparing with other molybdenum-based catalysts for electrochemical organic compound oxidation, the  $\text{MoO}_2/\text{MoP}/\text{NF-140}$  exhibits excellent ECO performance (Table S6).

Fig. 4c-d display LSV curves and Tafel slopes of  $\text{MoO}_2/\text{MoP}/\text{NF}$  electrodes synthesized at different hydrothermal temperatures. The  $\text{MoO}_2/\text{MoP}/\text{NF-140}$  presents the overpotential of 123 mV ( $10 \text{ mA cm}^{-2}$ ) and Tafel slope of  $39.8 \text{ mV dec}^{-1}$  (Table S7), which is significantly smaller than those of  $\text{MoO}_2/\text{MoP}/\text{NF-100}$  (137 mV,  $52.4 \text{ mV dec}^{-1}$ ),  $\text{MoO}_2/\text{MoP}/\text{NF-120}$  (133 mV,  $48.4 \text{ mV dec}^{-1}$ ) and  $\text{MoO}_2/\text{MoP}/\text{NF-160}$  (128 mV,  $41.8 \text{ mV dec}^{-1}$ ). As compared to other electrode materials, the  $\text{MoO}_2/\text{MoP}/\text{NF-140}$  possesses lower overpotential at the same current density after normalization by BET surface area (Fig. S24), demonstrating its higher intrinsic activity. Moreover, the  $\text{MoO}_2/\text{MoP}/\text{NF-140}$  shows the highest  $C_{\text{dl}}$  value ( $82.5 \text{ mF cm}^{-2}$ ) as compared to other electrodes, thus reflecting that it exposes abundant active sites (Figs. 4e, S25) [51,52]. Furthermore, the  $\text{MoO}_2/\text{MoP}/\text{NF-140}$  exhibits the lowest charge transfer resistance ( $R_{\text{ct}}$ ,  $17.27 \Omega$ ) among all the tested electrodes, reflecting an efficient electron transfer (Fig. 4f, Table S7) [53]. From XRD, Raman and SEM results, the electrode materials prepared at low hydrothermal temperature (below  $120^\circ\text{C}$ ) are covered with cone-like nanorods with poor crystallinity. However, the morphology changes significantly at high temperature ( $160^\circ\text{C}$ ), which would lead to small surface area. The  $\text{MoO}_2/\text{MoP}/\text{NF-140}$  has good crystallinity and large surface area, thereby providing excellent electrochemical performance.

As compared to  $\text{MoO}_2/\text{NF}$ ,  $\text{MoP}/\text{NF}$  and  $\text{NF}$ ,  $\text{MoO}_2/\text{MoP}/\text{NF}$  shows

superior ECO activity with the lowest overpotential at  $10 \text{ mA cm}^{-2}$ , the lowest Tafel slope, the largest ECSA and the smallest  $R_{\text{ct}}$  (Figs. S26, S27, Table S8), demonstrating a synergistic effect between  $\text{MoO}_2$  and  $\text{MoP}$  during the ECO of PX. So far, great progress has been made in the ECO of benzyl alcohols to benzyl acids in alkaline systems [54,55]. However, the electrochemical synthesis of benzyl acids from benzyl aromatics is still a huge challenge because the carboxyl group is easier to be oxidized relative to the methyl C-H bond. In this work, it is the first report on the direct ECO of benzyl aromatic methyl groups to benzyl acids with high selectivity in an alkaline media.

### 3.3. Potential-driven surface reconstruction of $\text{MoO}_2/\text{MoP}$ precatalyst

Potential-dependent Raman spectra were collected in a three-electrode electrochemical cell to provide deep insights on the surface reconstruction of  $\text{MoO}_2/\text{MoP}/\text{NF}$  electrodes during ECO of PX. As shown in Fig. 5a, only a small peak at  $744 \text{ cm}^{-1}$  attributed to the Mo-O stretching vibration of  $\text{MoO}_2$  is detectable at the electrode surface without applied potential [43]. At  $0.9 \text{ V}$ , a new peak assigning to the  $\nu_4$  asymmetric stretching of  $\text{MoO}_4^{2-}$  appears at  $316 \text{ cm}^{-1}$ . With progressively increasing the applied potentials, the peak at  $744 \text{ cm}^{-1}$  becomes insignificant, while new peaks belonging to the Mo-O-Mo bending vibration,  $\nu_2$  asymmetric stretching of  $\text{MoO}_4^{2-}$  and  $\nu_4$  asymmetric stretching of  $\text{MoO}_4^{2-}$  occur at  $471, 833$  and  $891 \text{ cm}^{-1}$  respectively [56–58]. Meanwhile, the band at  $1065 \text{ cm}^{-1}$  corresponding to the  $\nu_3$  triply degenerated asymmetric mode of P-O bond becomes obvious [23]. The above-mentioned changes of typical Raman peaks demonstrate the simultaneous formation of  $\text{MoO}_4^{2-}$  and  $\text{PO}_4^{3-}$  with the potential applied. All the characteristic bands exhibit the strongest intensities at  $1.3 \text{ V}$ ,

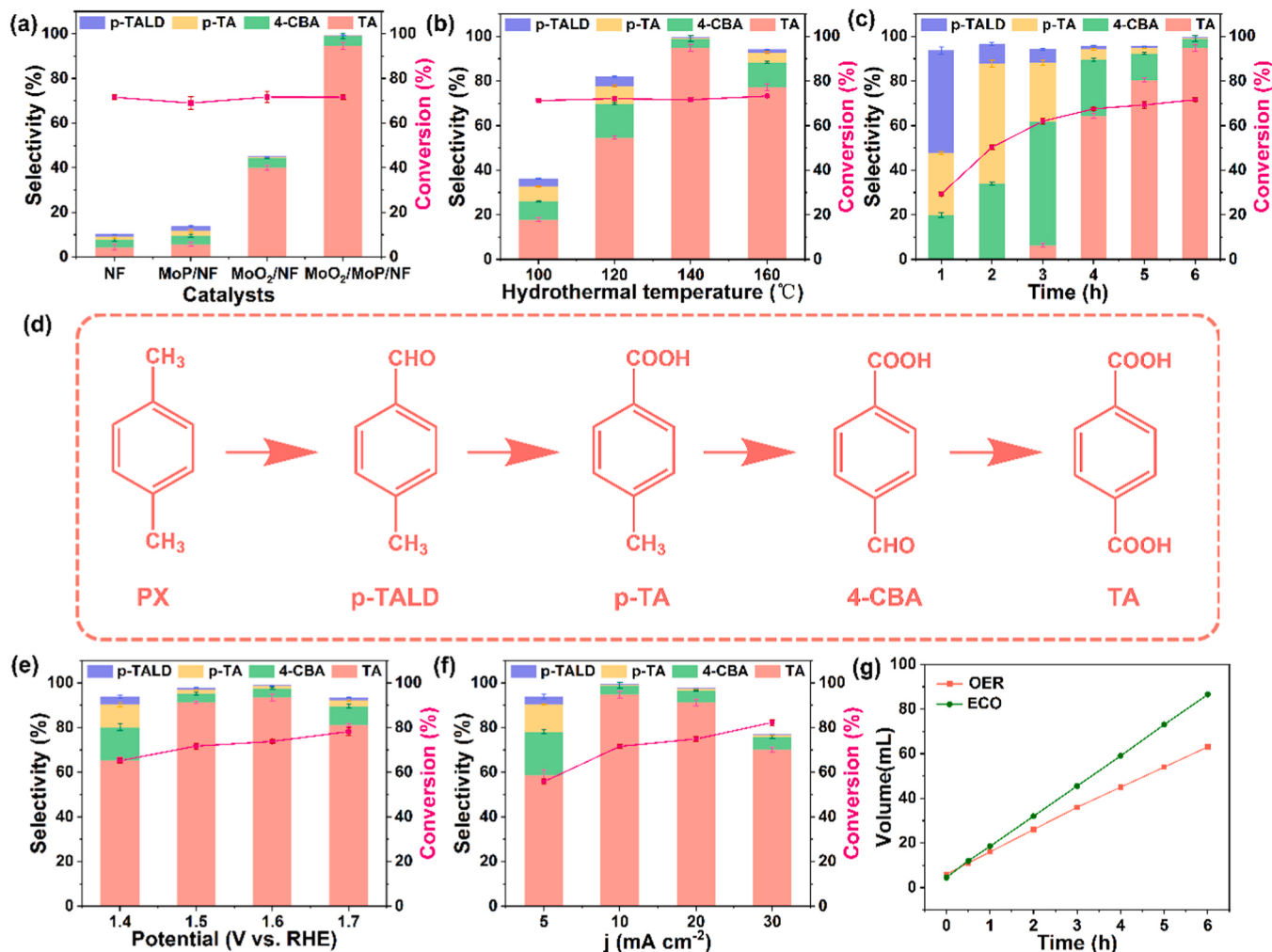


**Fig. 3.** (a) ECO of 25 mM PX over NF, MoP/NF, MoO<sub>2</sub>/NF and MoO<sub>2</sub>/MoP/NF electrodes for 6 h at 10 mA cm<sup>-2</sup>. (b) ECO of 25 mM PX over MoO<sub>2</sub>/MoP/NF-x electrodes for 6 h at 10 mA cm<sup>-2</sup>. (c) Effect of reaction time on ECO of 25 mM PX over MoO<sub>2</sub>/MoP/NF-140 at 10 mA cm<sup>-2</sup>. (d) Reaction pathway for ECO of PX. (e) Effect of applied potential on ECO of PX over MoO<sub>2</sub>/MoP/NF-140 for 6 h. (f) Effect of current density on ECO of 25 mM PX over MoO<sub>2</sub>/MoP/NF-140 for 6 h. (g) Amount of hydrogen as a function of reaction time under ECO (with 25 mM PX) and OER (without PX) conditions over MoO<sub>2</sub>/MoP/NF-140.

suggesting a complete surface reconstruction of the original electrode. Evidently, low valence Mo species in both MoP and MoO<sub>2</sub> undergo an anodic oxidation to form molybdate groups, while P species in MoP are also oxidized into phosphate groups during the ECO of PX. As a control, potential-dependent Raman spectra of the MoO<sub>2</sub>/NF electrode was shown in Fig. 5b. The electrode surface of MoO<sub>2</sub>/NF exhibit three typical peaks at 461, 496 and 746 cm<sup>-1</sup> assigned to MoO<sub>2</sub>. Under the applied potential, the features of MoO<sub>2</sub> disappear. In the meanwhile, the peaks corresponding to MoO<sub>4</sub><sup>2-</sup> and Mo-O-Mo gradually rise with the applied potential. This proves that MoO<sub>2</sub> also transforms into molybdate during the ECO process.

XRD and XPS were conducted to examine the surface structure of MoO<sub>2</sub>/MoP/NF-140 after potential-induced surface reconstruction. As shown in Fig. 5c, two crystalline phases of orthorhombic MoP<sub>2</sub>O<sub>8</sub> (PDF#16-0214) and triclinic K<sub>2</sub>Mo<sub>2</sub>O<sub>7</sub> (PDF#36-0347) can be observed after 2 h of reaction [59]. As the reaction time prolongs, the characteristic bands of both monoclinic MoO<sub>2</sub> and hexagonal MoP gradually disappear, whereas the diffraction features of both orthorhombic MoP<sub>2</sub>O<sub>8</sub> and triclinic K<sub>2</sub>Mo<sub>2</sub>O<sub>7</sub> phases become more pronounced. At 6 h, the sample contains mixed crystalline phases of orthorhombic MoP<sub>2</sub>O<sub>8</sub> and triclinic K<sub>2</sub>Mo<sub>2</sub>O<sub>7</sub>, proving that MoO<sub>2</sub> and MoP transform to MoP<sub>2</sub>O<sub>8</sub> and K<sub>2</sub>Mo<sub>2</sub>O<sub>7</sub>. Based on the analysis of crystallite size, the MoP phase of as-synthesized MoO<sub>2</sub>/MoP/NF disappears within 2 h of reaction, accompanied by the occurrence of the MoP<sub>2</sub>O<sub>8</sub> phase. Moreover,

the crystallite size of MoP<sub>2</sub>O<sub>8</sub> gradually increases as the reaction time prolongs. In the meanwhile, the crystallite size of MoO<sub>2</sub> phase progressively decreases while the mean size of K<sub>2</sub>Mo<sub>2</sub>O<sub>7</sub> significantly increases as ECO proceeds. This verifies a gradual transformation of physical phase during ECO process (Table S9). In addition, XRD pattern of post MoO<sub>2</sub>/NF (Fig. S28) indicates the conversion of MoO<sub>2</sub> to K<sub>2</sub>Mo<sub>2</sub>O<sub>7</sub> during ECO process. Obviously, the K<sub>2</sub>Mo<sub>2</sub>O<sub>7</sub> phase generated from surface reconstruction of MoO<sub>2</sub>/NF exhibits significant peaks at 24.4°, 26.9°, 28.7°, 36.4°, 42.1° and 53.3° corresponding to (111), (210), (-211), (2-11), (23-1) and (041) planes, which are different from the main crystal planes of K<sub>2</sub>Mo<sub>2</sub>O<sub>7</sub> converted from MoO<sub>2</sub>/MoP/NF-140.

The high-resolution Mo 3d spectrum demonstrates that both MoP and Mo(IV) species in the as-synthesized electrode are oxidized into Mo (VI) species (Fig. 5d). The O 1s spectrum can be fitted into two B.E.s derived from Mo (VI)-O and P-O bonds, respectively (Fig. 5e). Moreover, the appearance of P-O bond indicates the oxidation-induced transformation of Mo-P into Mo-P-O (Fig. 5f) [31,46,60]. It is worth noting that the B.E.s for K 2p and K 2s are detectable for the post electrode (Fig. S29), further confirming the formation of K<sub>2</sub>Mo<sub>2</sub>O<sub>7</sub> phase. It is evident that the electrode surface achieves the complete transformation of electronic states of Mo, O and P elements after 2 h of reaction. Nevertheless, MoO<sub>2</sub> and MoP completely convert to MoP<sub>2</sub>O<sub>8</sub> and K<sub>2</sub>Mo<sub>2</sub>O<sub>7</sub> after ECO of 6 h, which could be ascribed to the reconstitution

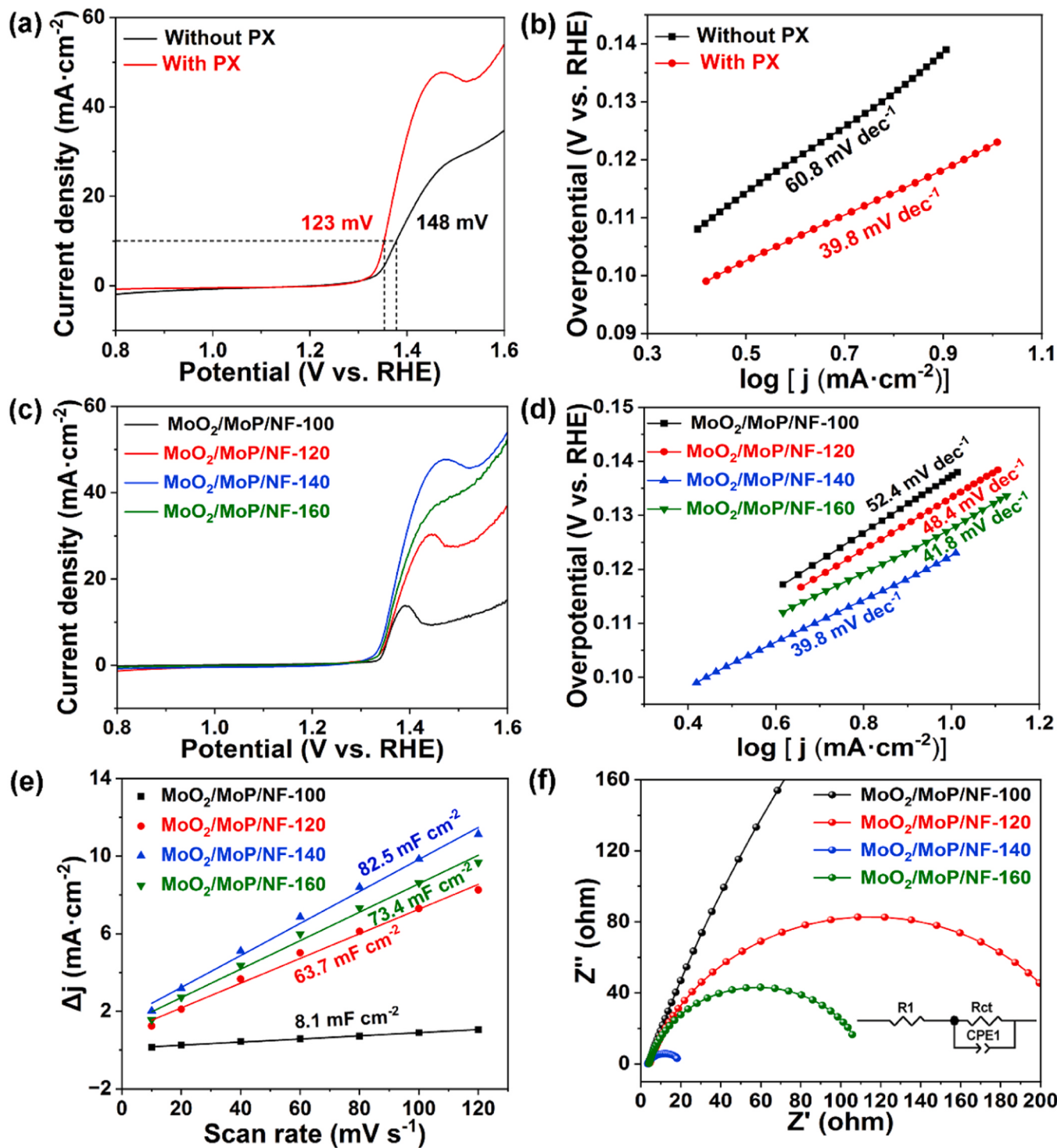


**Fig. 4.** (a) LSV curves, (b) Tafel slope plots of  $\text{MoO}_2/\text{MoP}/\text{NF}-140$  in 1 M KOH containing 30%  $\text{CH}_3\text{CN}$  ( $V_{\text{CH}_3\text{CN}}:V_{\text{H}_2\text{O}} = 3/7$ ) with and without PX. (c) LSV curves, (d) Tafel slope plots, (e) Double-layer capacitance ( $C_{dl}$ ) and (f) EIS Nyquist plots of the  $\text{MoO}_2/\text{MoP}/\text{NF}-x$  electrodes in 1 M KOH containing 30%  $\text{CH}_3\text{CN}$  ( $V_{\text{CH}_3\text{CN}}:V_{\text{H}_2\text{O}} = 3/7$ ) with 25 mM PX.

of bulk phase [31].

With prolonging the reaction time, the nancone-covered surface becomes smooth (Fig. 6a-d). The  $\text{MoO}_2/\text{MoP}/\text{NF}-140$  after ECO of 6 h presents the lattice spacing of 0.243 nm and 0.226 nm, which are consistent with the (202) crystal plane of  $\text{MoP}_2\text{O}_8$  and the (32-1) plane of  $\text{K}_2\text{Mo}_2\text{O}_7$ , respectively (Fig. 6e-g) [59]. The SAED pattern comprises rings attributable to  $\text{MoP}_2\text{O}_8$  and  $\text{K}_2\text{Mo}_2\text{O}_7$  (Fig. 6h). For comparison, cluster-like morphology of  $\text{MoO}_2/\text{NF}-140$  turns flat after reaction for 6 h

(Fig. S30). The lattice spacing for post  $\text{MoO}_2/\text{NF}-140$  is in good agreement with the (2-11) plane of  $\text{K}_2\text{Mo}_2\text{O}_7$  (Fig. S31).

Previous studies have reported that Mo-based anodic electrocatalysts are susceptible to be oxidized and leached to molybdate ( $\text{MoO}_4^{2-}$ ,  $\text{K}_2\text{MoO}_4$  or  $\text{K}_2\text{Mo}_3\text{O}_{10}$ ) in KOH during surface reconstruction [61]. These transformed molybdates can not only enhance the reconstruction degree of pre-catalyst into active phase, but also regulate the electronic conductivity of electrode material [62,63]. P species as pre-catalysts have

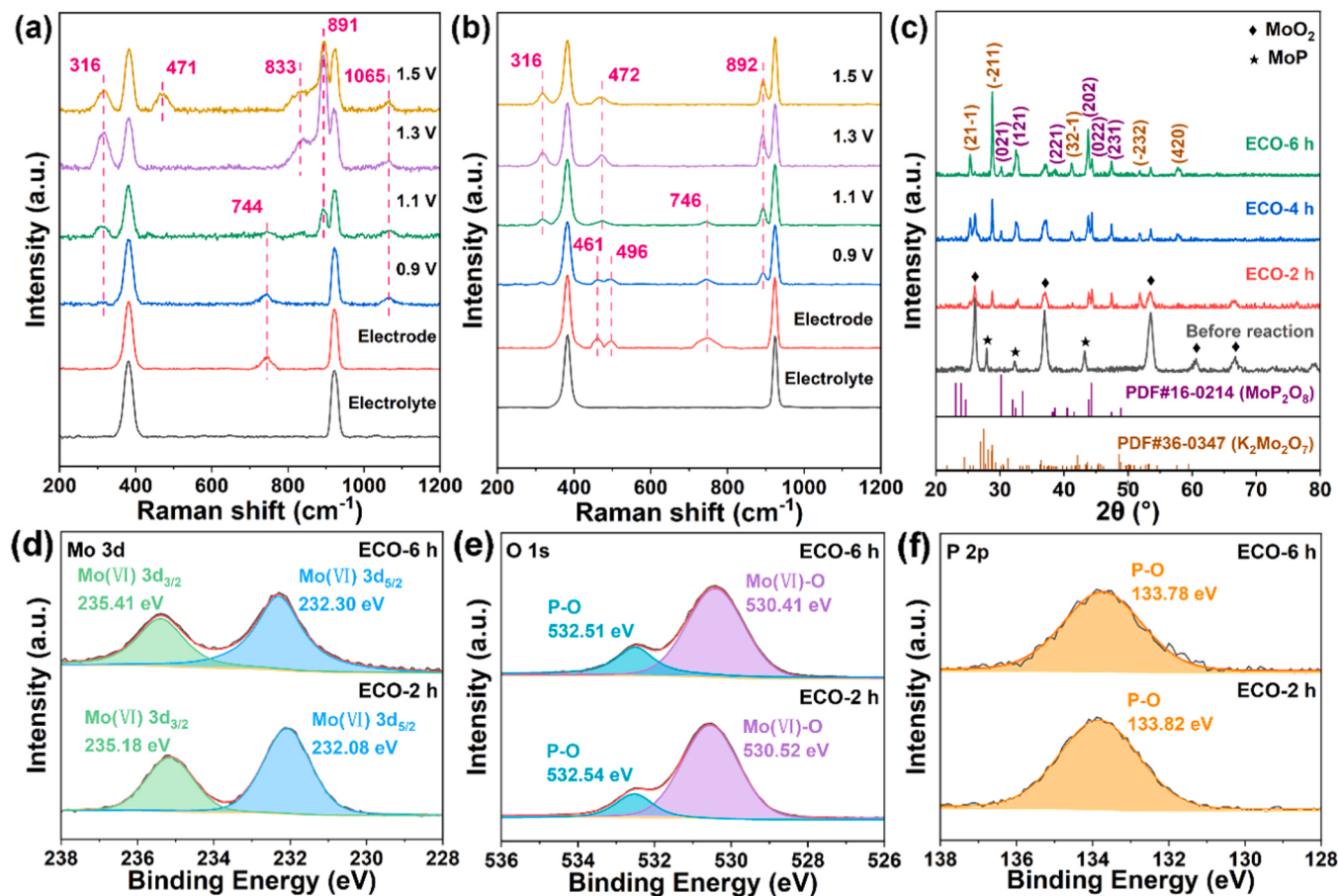


**Fig. 5.** *In-situ* Raman spectra of (a) MoO<sub>2</sub>/MoP/NF-140 and (b) MoO<sub>2</sub>/NF-140 in 1 M KOH containing 30% CH<sub>3</sub>CN (V<sub>CH3CN</sub>: V<sub>H2O</sub> = 3/7) with 25 mM PX at different applied potentials (V vs. RHE). (c) XRD patterns of MoO<sub>2</sub>/MoP/NF-140 after ECO at different reaction time. High-resolution XPS spectra for MoO<sub>2</sub>/MoP/NF-140 after ECO: (d) Mo 3d, (e) O 1s, (f) P 2p.

also been demonstrated to form oxygen-rich phosphide and further leach to phosphates under anodic potential. The leached P species with etching effect can promote the lattice distortion, improve interfacial charge transfer as well as enhance active surface area [31,64]. In this study, the MoO<sub>2</sub>/MoP hybrid undergoes a dynamic reconstitution to generate high-valent Mo species and P species. Partial leached Mo species form molybdate phase (K<sub>2</sub>Mo<sub>2</sub>O<sub>7</sub>) in KOH electrolyte, whereas the rest of Mo and P species are co-reconstructed to produce phosphomolybdate phase (MoP<sub>2</sub>O<sub>8</sub>).

### 3.4. Reaction mechanism for ECO of PX

DFT calculations were performed to unveil the reaction mechanism for ECO of PX over reconstructed MoP<sub>2</sub>O<sub>8</sub> and K<sub>2</sub>Mo<sub>2</sub>O<sub>7</sub> phases. According to XRD and HRTEM analysis (Figs. 5c, 6f-g), the (202) crystal plane of MoP<sub>2</sub>O<sub>8</sub> and the (32-1) crystal plane of K<sub>2</sub>Mo<sub>2</sub>O<sub>7</sub> were selected to represent the surface structure of MoO<sub>2</sub>/MoP after potential-driven reconstitution (Fig. S32). It is widely reported that the proton of methyl group of PX is easily abstracted by hydroxyl radicals to form p-methylbenzyl radicals (C<sub>7</sub>H<sub>7</sub>CH<sub>2</sub><sup>·</sup>) on the catalyst surface in PX-CH<sub>3</sub>CN-H<sub>2</sub>O system [65,66]. Consequently, the adsorption energy of C<sub>7</sub>H<sub>7</sub>CH<sub>2</sub><sup>·</sup> on the (202) plane of MoP<sub>2</sub>O<sub>8</sub> and (32-1) plane of K<sub>2</sub>Mo<sub>2</sub>O<sub>7</sub> were calculated respectively. The C<sub>7</sub>H<sub>7</sub>CH<sub>2</sub><sup>·</sup> radical adsorbs on MoP<sub>2</sub>O<sub>8</sub> via top oxygen sites (Fig. S33) with the adsorption energy of -2.37 eV (Fig. 7a). However, the adsorption energy of C<sub>7</sub>H<sub>7</sub>CH<sub>2</sub><sup>·</sup> adsorbed on K<sub>2</sub>Mo<sub>2</sub>O<sub>7</sub> via top oxygen sites is only -1.70 eV (Table S10), which is much lower than that on MoP<sub>2</sub>O<sub>8</sub>. Further, the adsorption energies of different intermediates and products on MoP<sub>2</sub>O<sub>8</sub> were compared. The

p-TALD (-0.44 eV), p-TA (-0.56 eV) and 4-CBA (-0.48 eV) prefer to adsorb on MoP<sub>2</sub>O<sub>8</sub> with the formyl groups located on top P sites (Fig. S34), whereas TA adsorbs weakly on MoP<sub>2</sub>O<sub>8</sub> (-0.13 eV). It is suggested that TA is liable to desorb from the catalyst surface (Table S11).

In order to elucidate the critical role of P, the adsorption energies of different intermediates and products on the (2-11) crystal plane of K<sub>2</sub>Mo<sub>2</sub>O<sub>7</sub> (the dominant crystal plane for post MoO<sub>2</sub>/NF) were also calculated (Fig. 7b, Table S12). All the intermediates and products are strongly adsorbed on the (2-11) plane of K<sub>2</sub>Mo<sub>2</sub>O<sub>7</sub> between Mo sites and methylene or formyl groups (Fig. S35). Accordingly, the strong adsorption between TA and Mo makes it difficult to desorb from the catalyst surface, which would lead to an over-oxidation of TA. Hence, it can be reasonably concluded that the doping of P can significantly reduce the adsorption of TA (-1.43 eV to -0.13 eV, Fig. 7c-d) and effectively improve the selectivity.

XPS analysis demonstrates that the MoO<sub>2</sub>/MoP/NF-140 contains the highest proportion of MoP (Table S3). From the ECO results, the MoO<sub>2</sub>/MoP/NF-140 exhibits considerably higher TA selectivity (94.8%) as compared to MoO<sub>2</sub>/MoP/NF-100 (17.8%), MoO<sub>2</sub>/MoP/NF-120 (54.6%) and MoO<sub>2</sub>/MoP/NF-160 (77.3%), indicating that high proportion of MoP is favorable for high selectivity of TA. DFT calculations demonstrate that the top P site on the phosphomolybdate surface facilitates the adsorption of reaction intermediates but weakens the adsorption of TA. Therefore, MoO<sub>2</sub>/MoP/NF-140 with the highest content of MoP may lead to abundant P sites on catalyst surface, thus effectively improving the selectivity of TA.

The catalytic mechanism for ECO of PX is proposed in Fig. 7e. The

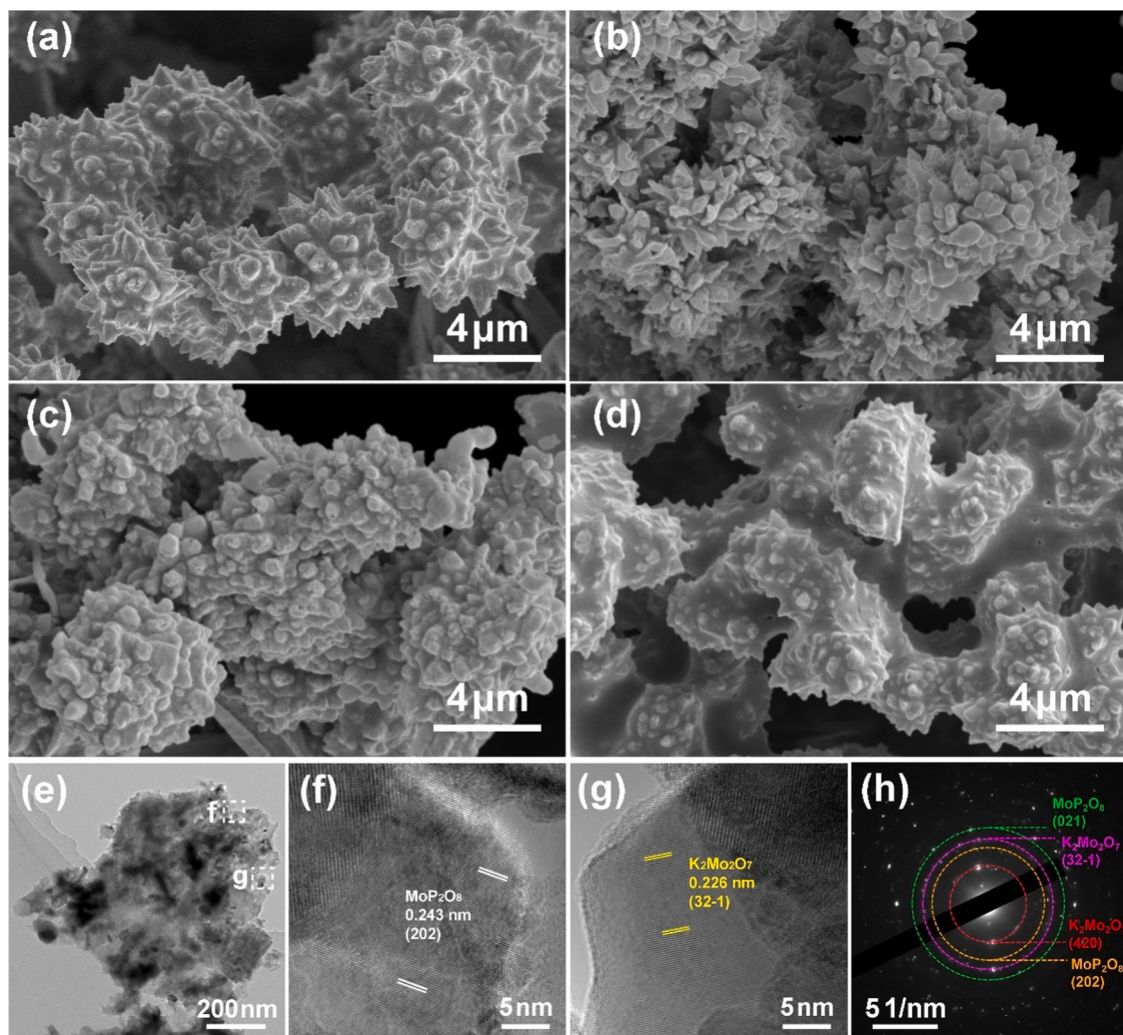


**Fig. 6.** SEM images of  $\text{MoO}_2/\text{MoP}/\text{NF-140}$  before (a) and after reaction for (b) 2 h, (c) 4 h, (d) 6 h. (e) TEM image, (f, g) HRTEM images and (h) SAED pattern of  $\text{MoO}_2/\text{MoP}/\text{NF-140}$  after reaction for 6 h.

surface of  $\text{MoO}_2/\text{MoP}/\text{NF}$  derives into  $\text{MoP}_2\text{O}_8$  and  $\text{K}_2\text{Mo}_2\text{O}_7$  phases via potential-induced surface reconstruction. Initially, the methyl group of PX undergoes a hydrogen abstraction to form  $\text{C}_7\text{H}_7\text{CH}_2\cdot$  radical. The  $\text{MoP}_2\text{O}_8$  surface modulates the adsorption strength of reaction intermediates involving p-TALD, p-TA and 4-CBA, mainly through the top P sites. Furthermore, it also weakens the adsorption strength of TA on the electrode surface, thereby facilitating the desorption of TA. For comparison, the  $\text{MoO}_2/\text{NF}$  without P doping converts to  $\text{K}_2\text{Mo}_2\text{O}_7$  phase driven by electrochemical oxidation. Both reaction intermediates and oxidized product exhibit strong adsorption strength on the electrode surface via Mo sites, giving relatively low selectivity toward TA.

#### 4. Conclusion

In summary, a facile hydrothermal-phosphorylation method was developed to fabricate hybrid  $\text{MoO}_2/\text{MoP}/\text{NF}$  electrode materials for ECO of PX in alkaline environment. The crystalline structures and morphologies of  $\text{MoO}_2/\text{MoP}$  precatalysts are highly dependent upon hydrothermal temperatures. The optimal electrocatalyst exhibits nano-cone cluster-like architecture, resulting in outstanding electrochemical performance during ECO of PX such as large electrochemical surface area, highly exposed active sites and rapid charge transfer kinetics during ECO of PX. The ECO of PX gives the TA selectivity of 94.8% and faradaic efficiency of 76.9% at the PX conversion of 71.6%. As compared to OER process, the anodic oxidation of PX promotes the cathodic

hydrogen production by 30%. Moreover, PX electro-oxidation assisted water electrolysis requires only 1.42 V to drive  $10 \text{ mA cm}^{-2}$  with a superior stability over 40 h. *In-situ* Raman and DFT calculations unravel the dynamic surface reconstruction of  $\text{MoO}_2/\text{MoP}/\text{NF}$  pre-catalyst during ECO of PX. New crystalline phases of  $\text{MoP}_2\text{O}_8$  and  $\text{K}_2\text{Mo}_2\text{O}_7$  simultaneously form during potential-driven *in-situ* reconstitution of  $\text{MoO}_2/\text{MoP}$  pre-catalyst. The top P sites on the (202) plane of  $\text{MoP}_2\text{O}_8$  adjust the adsorption energies of p-TALD, p-TA and 4-CBA. The  $\text{MoP}_2\text{O}_8$  surface also weaken the adsorption strength of TA, thereby contributing to high selectivity. For comparison, electrocatalytically generated  $\text{K}_2\text{Mo}_2\text{O}_7$  phase on the  $\text{MoO}_2/\text{NF}$  without P doping shows low selectivity probably due to large adsorption energy of TA on the dominant crystal plane. This work clarifies the role of P element of transition-metal phosphide during ECO of organic compounds and opens up a new path to explore the real active sites of electrocatalysts for valuable chemicals production via potential-induced surface reconstruction.

#### CRediT authorship contribution statement

**Ye Lv:** Methodology, Investigation, Writing – original draft. **Mao Peng:** Software, Density functional theory (DFT) calculations. **Weiwei Yang:** Methodology, Investigation. **Menghui Liu:** Visualization. **Aiqun Kong:** Methodology, Data curation. **Yan Fu:** Conceptualization, Writing – review & editing. **Wei Li:** Resources, Supervision, Writing – review & editing. **Jinli Zhang:** Project administration, Funding acquisition,

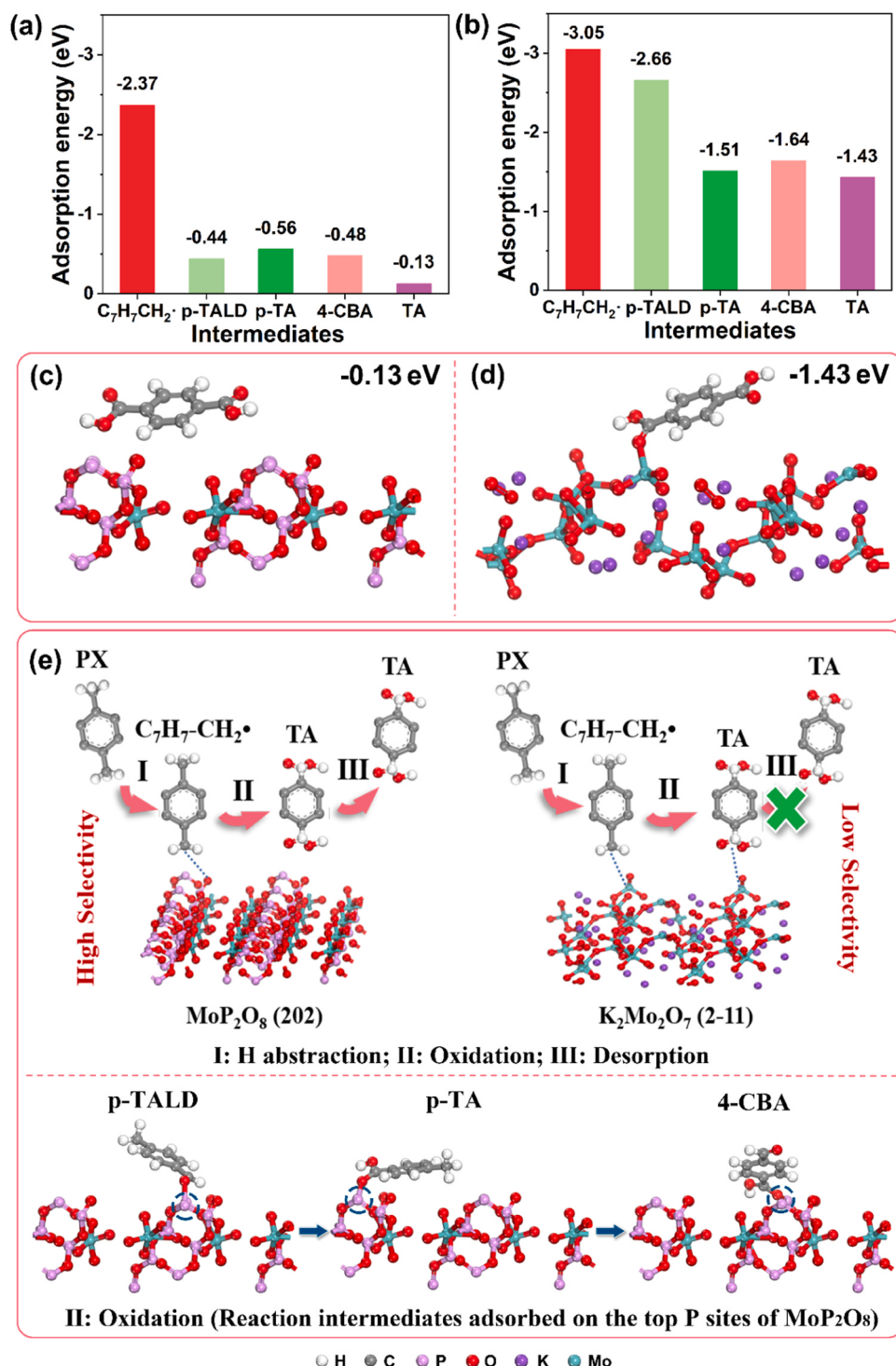


**Fig. 7.** The adsorption energies (eV) of different intermediates on (a) the (202) crystal plane of  $\text{MoP}_2\text{O}_8$ , (b) the (2-11) crystal plane of  $\text{K}_2\text{Mo}_2\text{O}_7$ . Ball and stick model of adsorption of TA on (c) the (202) crystal plane of  $\text{MoP}_2\text{O}_8$ , (d) the (2-11) crystal plane of  $\text{K}_2\text{Mo}_2\text{O}_7$ . (e) Illustration of the mechanism for ECO of PX.

Writing – review & editing. All authors have read and agreed to the published version of the manuscript.

#### Declaration of Competing Interest

The authors declare that they have no known competing financial interests or personal relationships that could have appeared to influence the work reported in this paper.

#### Data availability

No data was used for the research described in the article.

#### Acknowledgments

This work was financially supported by NSFC (No. 22090034, U20A20151), the National Key Research and Development Program (2021YFB4000303).

## Appendix A. Supporting information

Supplementary data associated with this article can be found in the online version at [doi:10.1016/j.apcatb.2023.123229](https://doi.org/10.1016/j.apcatb.2023.123229).

## References

- B. You, Y.J. Sun, Innovative strategies for electrocatalytic water splitting, *Acc. Chem. Res.* 51 (2018) 1571–1580, <https://doi.org/10.1021/acs.accounts.8b00002>.
- T.Z. Wang, X.J. Cao, L.F. Jiao, Progress in hydrogen production coupled with electrochemical oxidation of small molecules, *Angew. Chem. Int. Ed.* 61 (2022), e202213328, <https://doi.org/10.1002/anie.202213328>.
- H.-Y. Wang, M.-L. Sun, J.-T. Ren, Z.-Y. Yuan, Circumventing challenges: design of anodic electrocatalysts for hybrid water electrolysis systems, *Adv. Energy Mater.* 13 (2023), 2203568, <https://doi.org/10.1002/aenm.202203568>.
- M.Q. Yu, E. Budiyanto, H. Tuysuz, Principles of water electrolysis and recent progress in cobalt-, nickel-, and iron-based oxides for the oxygen evolution reaction, *Angew. Chem. Int. Ed.* 61 (2022), e202103824, <https://doi.org/10.1002/anie.202103824>.
- F.Y. Chen, Z.Y. Wu, Z. Adler, H.T. Wang, Stability challenges of electrocatalytic oxygen evolution reaction: from mechanistic understanding to reactor design, *Joule* 5 (2021) 1704–1731, <https://doi.org/10.1016/j.joule.2021.05.005>.
- Z.X. Li, M.L. Hu, P. Wang, J.H. Liu, J.S. Yao, C.Y. Li, Heterojunction catalyst in electrocatalytic water splitting, *Coord. Chem. Rev.* 439 (2021), <https://doi.org/10.1016/j.ccr.2021.213953>.
- H.J. Zhang, A.W. Maijenburg, X.P. Li, S.L. Schweizer, R.B. Wehrspohn, Bifunctional heterostructured transition metal phosphides for efficient electrochemical water splitting, *Adv. Funct. Mater.* 30 (2020), 2003261, <https://doi.org/10.1002/adfm.202003261>.
- C.A. Zhou, S.H. Wang, K. Ma, L. Song, L.R. Zheng, H.R. Yue, Membrane-free pure H<sub>2</sub> production over single dispersed Ru-anchored Pt<sub>3</sub>Ni alloys via coupling ethanol selective electrooxidation, *Appl. Catal. B Environ.* 321 (2023), 122065, <https://doi.org/10.1016/j.apcatb.2022.122065>.
- J. Wan, X. Mu, Y. Jin, J.K. Zhu, Y.C. Xiong, T.Y. Li, R. Li, Nitrogen-doped nickel-molybdenum oxide as a highly efficient electrocatalyst for benzyl alcohol oxidation, *Green Chem.* 24 (2022) 4870–4876, <https://doi.org/10.1039/d2gc00989g>.
- S.L. Fereja, P. Li, Z.W. Zhang, J.H. Guo, Z.Y. Fang, Z.J. Li, S.J. He, W. Chen, W-doping induced abundant active sites in a 3D NiS<sub>2</sub>/MoO<sub>3</sub> heterostructure as an efficient electrocatalyst for urea oxidation and hydrogen evolution reaction, *Chem. Eng. J.* 432 (2022), 134274, <https://doi.org/10.1016/j.cej.2021.134274>.
- M. Li, X.D. Wu, K. Liu, Y.F. Zhang, X.C. Jiang, D.M. Sun, Y.W. Tang, K. Huang, G. Tu, Nitrogen vacancies enriched Ce-doped Ni<sub>3</sub>N hierarchical nanosheets triggering highly-efficient urea oxidation reaction in urea-assisted energy-saving electrolysis, *J. Energy Chem.* 69 (2022) 506–515, <https://doi.org/10.1016/j.jec.2022.01.031>.
- Q.Z. Qian, J.H. Zhang, J.M. Li, Y.P. Li, X. Jin, Y. Zhu, Y. Liu, Z.Y. Li, A. El-Harairy, C. Xiao, G.Q. Zhang, Y. Xie, Artificial heterointerfaces achieve delicate reaction kinetics towards hydrogen evolution and hydrazine oxidation catalysis, *Angew. Chem. Int. Ed.* 60 (2021) 5984–5993, <https://doi.org/10.1002/anie.202014362>.
- F. Sun, D. He, K. Yang, J. Qiu, Z. Wang, Hydrogen production and water desalination with on-demand electricity output enabled by electrochemical neutralization chemistry, *Angew. Chem. Int. Ed.* 61 (2022), e202203929, <https://doi.org/10.1002/anie.202203929>.
- C. Liu, X.-R. Shi, K. Yue, P. Wang, K. Zhan, X. Wang, B.Y. Xia, Y. Yan, S-species-evoked high-valence Ni<sup>2+–8</sup> of the evolved  $\beta$ -Ni(OH)<sub>2</sub> electrode for selective oxidation of 5-hydroxymethylfurfural, *Adv. Mater.* 35 (2023), 2211177, <https://doi.org/10.1002/adma.202211177>.
- S.W. Yang, Y. Guo, Y.K. Zhao, L. Zhang, H.D. Shen, J.H. Wang, J.J. Li, C. Wu, W. B. Wang, Y.L. Cao, S.F. Zhuo, Q.Y. Zhang, H.P. Zhang, Construction of synergistic Ni<sub>3</sub>S<sub>2</sub>–MoS<sub>2</sub> nanoheterojunctions on Ni foam as bifunctional electrocatalyst for hydrogen evolution integrated with biomass valorization, *Small* 18 (2022), 2201306, <https://doi.org/10.1002/smll.202201306>.
- L.F. Fan, Y.X. Ji, G.X. Wang, J.X. Chen, K. Chen, X. Liu, Z.H. Wen, High entropy alloy electrocatalytic electrode toward alkaline glycerol valorization coupling with acidic hydrogen production, *J. Am. Chem. Soc.* 144 (2022) 7224–7235, <https://doi.org/10.1021/jacs.1c13740>.
- G.B. Chen, X.D. Li, X.L. Feng, Upgrading organic compounds through the coupling of electrooxidation with hydrogen evolution, *Angew. Chem. Int. Ed.* 61 (2022), e202209014, <https://doi.org/10.1002/anie.202209014>.
- Z.H. Li, X.F. Li, H. Zhou, Y. Xu, S.M. Xu, Y. Ren, Y.F. Yan, J.R. Yang, K.Y. Ji, L. Li, M. Xu, M.F. Shao, X.G. Kong, X.M. Sun, H.H. Duan, Electrocatalytic synthesis of adipic acid coupled with H<sub>2</sub> production enhanced by a ligand modification strategy, *Nat. Commun.* 13 (2022) 5009, <https://doi.org/10.1038/s41467-022-32769-0>.
- L. Xu, D.W. Chen, H. Jiang, X. Yuan, Efficient oxidation of p-xylene to terephthalic acid by using N,N-dihydroxypyromellitimide in conjunction with Co-benzenetricarboxylate, *Appl. Catal. A Gen.* 599 (2020), 117569, <https://doi.org/10.1016/j.apcata.2020.117569>.
- T.L.Zhang Xuechao, Xie Yongchao, Zhang Jishu, Studies on preparation of terephthalic acid by indirect electro-oxidation using Cr(VI) as oxidic medium, *J. Qing Dao Univ. Sci. Technol.* 27 (2006) 104–107.
- M. Balagangesh, S. Lawrence, C. Christopher, A.J. Bosco, K. Kulangiappar, K.J. S. Raj, Nitrate mediated oxidation of p-xylene by emulsion electrolysis, *Electrochim. Acta* 111 (2013) 384–389, <https://doi.org/10.1016/j.electacta.2013.08.020>.
- J. Zhong, Y.L. Shen, P. Zhu, S. Yao, C.H. An, Size-effect on Ni electrocatalyst: the case of electrochemical benzyl alcohol oxidation, *Nano Res.* 16 (2023) 202–208, <https://doi.org/10.1007/s12274-022-4679-6>.
- H.L. Huang, C. Yu, X.T. Han, H.W. Huang, Q.B. Wei, W. Guo, Z. Wang, J.S. Qiu, Ni, Co hydroxide triggers electrocatalytic production of high-purity benzoic acid over 400 mA cm<sup>-2</sup>, *Energy Environ. Sci.* 13 (2020) 4990–4999, <https://doi.org/10.1039/dlee00060a>.
- T. Shen, Y.-L. Li, K.-Y. Ye, T.H. Lambert, Electrophotocatalytic oxygenation of multiple adjacent C–H bonds, *Nature* 614 (2023) 275–280, <https://doi.org/10.1038/s41586-022-05608-x>.
- C.A. Malapit, M.B. Prater, J.R. Cabrera-Pardo, M. Li, T.D. Pham, T.P. McFadden, S. Blank, S.D. Minteer, Advances on the merger of electrochemistry and transition metal catalysis for organic synthesis, *Chem. Rev.* 122 (2022) 3180–3218, <https://doi.org/10.1021/acs.chemrev.1c00614>.
- C.X. Zhao, J.N. Liu, J. Wang, C.D. Wang, X. Guo, X.Y. Li, X. Chen, L. Song, B.Q. Li, Q. Zhang, A clicking confinement strategy to fabricate transition metal single-atom sites for bifunctional oxygen electrocatalysis, *Sci. Adv.* 8 (2022) eabn5091, <https://doi.org/10.1126/sciadv.abn5091>.
- A. Zhang, Y.X. Liang, H. Zhang, Z.G. Geng, J. Zeng, Doping regulation in transition metal compounds for electrocatalysis, *Chem. Soc. Rev.* 50 (2021) 9817–9844, <https://doi.org/10.1039/dlcs00330e>.
- K.H. Yue, J.L. Liu, Y.T. Zhu, C.F. Xia, P. Wang, J.W. Zhang, Y. Kong, X.Y. Wang, Y. Yan, B.Y. Xia, *In situ* ion-exchange preparation and topological transformation of trimetal-organic frameworks for efficient electrocatalytic water oxidation, *Energy Environ. Sci.* 14 (2021) 6546–6553, <https://doi.org/10.1039/dlee02606b>.
- G. Xu, C.Y. Chen, M.X. Li, X.Y. Ren, L.G. Hu, C.R. Wu, Y. Zhuang, F.N. Wang, W exsolution promotes the *in situ* reconstruction of a NiW electrode with rich active sites for the electrocatalytic oxidation of 5-hydroxymethylfurfural (HMF), *Catal. Sci. Technol.* 12 (2022) 3363–3371, <https://doi.org/10.1039/d2cy00384h>.
- Z.P. Ma, C. Tsounis, C.Y. Toe, P.V. Kumar, B. Subhash, S.B. Xi, H.Y. Yang, S. J. Zhou, Z.H. Lin, K.H. Wu, R.J. Wong, L. Thomsen, N.M. Bedford, X.Y. Lu, Y.H. Ng, Z.J. Han, R. Amal, Reconstructing Cu nanoparticle supported on vertical graphene surfaces via electrochemical treatment to tune the selectivity of CO<sub>2</sub> reduction toward valuable products, *ACS Catal.* 12 (2022) 4792–4805, <https://doi.org/10.1021/acscatal.1c05431>.
- X. Han, C. Yu, Y. Niu, Z. Wang, Y. Kang, Y. Ren, H. Wang, H.S. Park, J. Qiu, Full bulk-structure reconstruction into amorphized cobalt-iron oxyhydroxide nanosheet electrocatalysts for greatly improved electrocatalytic activity, *Small Methods* 4 (2020), 2000546, <https://doi.org/10.1002/smtd.202000546>.
- H.L. Wang, C. Li, J.T. An, Y. Zhuang, S.Y. Tao, Surface reconstruction of NiCoP for enhanced biomass upgrading, *J. Mater. Chem. A* 9 (2021) 18421–18430, <https://doi.org/10.1039/dta105425b>.
- F.H. Hsu, S.Y. Hsu, B.H. Chen, J.L. Chen, J.M. Chen, K.T. Lu, Correlation of the crystal structure and ion storage behavior of MoO<sub>3</sub> electrode materials for aluminum-ion energy storage studied using *in situ* X-ray spectroscopy, *Nanoscale* 14 (2022) 7502–7515, <https://doi.org/10.1039/d2nr00182a>.
- F.J. Lesafi, T. Pogrebnyak, C.K. King, Effect of the calcination temperature on SnO<sub>2</sub>–MoO<sub>3</sub> crystal structure and catalytic activity in desulfurization of model diesel, *Fuel* 330 (2022), 125601, <https://doi.org/10.1016/j.fuel.2022.125601>.
- A. Saraeian, S.J. Burkhow, D.P. Jing, E.A. Smith, B.H. Shanks, Catalyst property effects on product distribution during the hydrodeoxygenation of lignin pyrolysis vapors over MoO<sub>3</sub>/gamma-Al<sub>2</sub>O<sub>3</sub>, *ACS Sustain. Chem. Eng.* 9 (2021) 6685–6696, <https://doi.org/10.1021/acssuschemeng.1c00295>.
- H. Hu, I.E. Wachs, Catalytic properties of supported molybdenum oxide catalysts: *in situ* Raman and methanol oxidation studies, *J. Phys. Chem. C* 99 (1995) 10911–10922, <https://doi.org/10.1021/j100027a035>.
- L.-p. Hou, R.-x. Zhao, X.-p. Li, X.-h. Gao, Preparation of MoO<sub>2</sub>/g-C<sub>3</sub>N<sub>4</sub> composites with a high surface area and its application in deep desulfurization from model oil, *Appl. Surf. Sci.* 434 (2018) 1200–1209, <https://doi.org/10.1016/j.apsusc.2017.10.076>.
- U. Kumar Sen, A. Shaligram, S. Mitra, Intercalation anode material for lithium ion battery based on molybdenum dioxide, *ACS Appl. Mater. Interfaces* 6 (2014) 14311–14319, <https://doi.org/10.1021/am503605u>.
- B.P. Thapaliya, E.C. Self, C.J. Jafra, A.Y. Borisevich, H.M. Meyer III, C.A. Bridges, J. Nanda, S. Dai, Synthesizing high-capacity oxyfluoride conversion anodes by direct fluorination of molybdenum dioxide (MoO<sub>2</sub>), *ChemSusChem* 13 (2020) 3825–3834, <https://doi.org/10.1002/cssc.202001006>.
- B. Long, J. Ma, T. Song, S. Song, Y. Tong, X. Wang, Intercalation-type MoP and WP nanodots with abundant phase interface embedded in carbon microflower for enhanced Li storage and reaction kinetics, *Electrochim. Acta* 365 (2021), 137354, <https://doi.org/10.1016/j.electacta.2020.137354>.
- C.-C. Hou, L. Zou, Y. Wang, Q. Xu, MOF-mediated fabrication of a porous 3D superstructure of carbon nanosheets decorated with ultrafine cobalt phosphide nanoparticles for efficient electrocatalysis and zinc-air batteries, *Angew. Chem. Int. Ed.* 59 (2020) 21360–21366, <https://doi.org/10.1002/anie.202011347>.
- P. Xu, W. Zhao, X. Liu, B. Jia, J. He, L. Fu, B. Xu, Dramatic enhancement of thermoelectric performance in PbTe by unconventional grain shrinking in the sintering process, *Adv. Mater.* 34 (2022), 2202949, <https://doi.org/10.1002/adma.202202949>.
- W. Marquart, S. Raseale, G. Prieto, A. Zimina, B.B. Sarma, J.-D. Grunwaldt, M. Claeys, N. Fischer, CO<sub>2</sub> reduction over Mo<sub>2</sub>C-based catalysts, *ACS Catal.* 11 (2021) 1624–1639, <https://doi.org/10.1021/acscatal.0c05019>.

[44] M. He, H. Shi, X. Sun, B. Gao, Porous Mo<sub>2</sub>C-MoP heterostructure on carbon cloth for efficient hydrogen evolution reaction over a broad pH range, *ChemCatChem* 13 (2021) 966–974, <https://doi.org/10.1002/cctc.202001639>.

[45] F. Chen, B. Zhao, M. Sun, C. Liu, Y. Shi, Y. Yu, B. Zhang, Mechanistic insight into the controlled synthesis of metal phosphide catalysts from annealing of metal oxides with sodium hypophosphite, *Nano Res.* 15 (2022) 10134–10141, <https://doi.org/10.1007/s12274-022-4489-x>.

[46] Y. Zhang, S.-J. Park, Phosphorization-derived MoP@MoO<sub>3</sub>-x nanowires for selective photocatalytic oxidation of benzyl alcohol to benzaldehyde, *J. Catal.* 394 (2021) 332–341, <https://doi.org/10.1016/j.jcat.2020.11.001>.

[47] H. Salari, J.S. Shayeh, A unique 3D structured NiMoO<sub>4</sub>/MoO<sub>3</sub> heterojunction for enhanced supercapacitor performance, *Energy Fuels* 35 (2021) 16144–16151, <https://doi.org/10.1021/acs.energyfuels.1c01793>.

[48] G. Yang, Y. Jiao, H. Yan, Y. Xie, A. Wu, X. Dong, D. Guo, C. Tian, H. Fu, Interfacial engineering of MoO<sub>2</sub>-FeP heterojunction for highly efficient hydrogen evolution coupled with biomass electrooxidation, *Adv. Mater.* 32 (2020), 2000455, <https://doi.org/10.1002/adma.202000455>.

[49] M. Esmaeilirad, A. Kondori, N. Shan, M.T. Saray, S. Sarkar, A.M. Harzandi, C. M. Megaridis, R. Shahbazian-Yassar, L.A. Curtiss, C.U. Segre, M. Asadi, Efficient electrocatalytic conversion of CO<sub>2</sub> to ethanol enabled by imidazolium-functionalized ionomer confined molybdenum phosphide, *Appl. Catal. B Environ.* 317 (2022), 121681, <https://doi.org/10.1016/j.apcatb.2022.121681>.

[50] D. Chen, R. Lu, Z. Pu, J. Zhu, H.-W. Li, F. Liu, S. Hu, X. Luo, J. Wu, Y. Zhao, S. Mu, Ru-doped 3D flower-like bimetallic phosphide with a climbing effect on overall water splitting, *Appl. Catal. B Environ.* 279 (2020), 119396, <https://doi.org/10.1016/j.apcatb.2020.119396>.

[51] J. Li, Y. Li, J. Wang, C. Zhang, H. Ma, C. Zhu, D. Fan, Z. Guo, M. Xu, Y. Wang, H. Ma, Elucidating the critical role of ruthenium single atom sites in water dissociation and dehydrogenation behaviors for robust hydrazine oxidation-boosted alkaline hydrogen evolution, *Adv. Funct. Mater.* 32 (2022), 2109439, <https://doi.org/10.1002/adfm.202109439>.

[52] J. Kang, X. Qiu, Q. Hu, J. Zhong, X. Gao, R. Huang, C. Wan, L.-M. Liu, X. Duan, L. Guo, Valence oscillation and dynamic active sites in monolayer NiCo hydroxides for water oxidation, *Nat. Catal.* 4 (2021) 1050–1058, <https://doi.org/10.1038/s41929-021-00715-w>.

[53] A.Q. Kong, M. Peng, M.H. Liu, Y. Lv, H.J. Zhang, Y.S. Gao, J. Liu, Y. Fu, W. Li, J. L. Zhang, Robust Pt/TiO<sub>2</sub>/Ni(OH)<sub>2</sub> nanosheet arrays enable outstanding performance for high current density alkaline water electrolysis, *Appl. Catal. B Environ.* 316 (2022), 121654, <https://doi.org/10.1016/j.apcatb.2022.121654>.

[54] T. Ali, H.Y. Wang, W. Iqbal, T. Bashir, R.H. Shah, Y. Hu, Electro-synthesis of organic compounds with heterogeneous catalysis, *Adv. Sci.* 10 (2023), 2205077, <https://doi.org/10.1002/advs.202205077>.

[55] Z. Li, Y. Yan, S.-M. Xu, H. Zhou, M. Xu, L. Ma, M. Shao, X. Kong, B. Wang, L. Zheng, H. Duan, Alcohols electrooxidation coupled with H<sub>2</sub> production at high current densities promoted by a cooperative catalyst, *Nat. Commun.* 13 (2022) 141–147, <https://doi.org/10.1038/s41467-021-27806-3>.

[56] L.H. Zhou, C.M. Yang, W.C. Zhu, R. Li, X.X. Pang, Y.Z. Zhen, C.T. Wang, L.J. Gao, F. Fu, Z.W. Gao, Y.C. Liang, Boosting alkaline hydrogen evolution reaction via an unexpected dynamic evolution of molybdenum and selenium on MoSe<sub>2</sub> electrode, *Adv. Energy Mater.* 12 (2022), 2202367, <https://doi.org/10.1002/aenm.202202367>.

[57] B. Binish, K.M. Rahulan, A. Dhanusha, T.C.S. Girisun, J.M. Laskar, Influence of yttrium doping on the nonlinear optical limiting properties of cadmium molybdate nanostructures, *RSC Adv.* 12 (2022) 27145–27153, <https://doi.org/10.1039/d2ra04687c>.

[58] P.N. Kumar, V. Ponnivalavan, W. Lee, J. Yoon, Zinc additions in calcium phosphate system. Phase behavior, microstructural and mechanical compatibility during sequential heat treatments, *J. Alloy. Compd.* 929 (2022), 167173, <https://doi.org/10.1016/j.jallcom.2022.167173>.

[59] G.D. Saraiva, L.F. Lobato, A.V.L. Ferreira, W. Paraguassu, A.J. Ramiro de Castro, R. F. Juçá, V.O. Sousa Neto, A.M.R. Teixeira, F.F. de Sousa, A temperature-dependent Raman scattering and X-ray diffraction study of K<sub>2</sub>Mo<sub>2</sub>O<sub>7</sub>-H<sub>2</sub>O and ab initio calculations of K<sub>2</sub>Mo<sub>2</sub>O<sub>7</sub>, *Spectrochim. Acta A* 263 (2021), 120184, <https://doi.org/10.1016/j.saa.2021.120184>.

[60] Y.H. Shen, Y.L. Jiang, Z.Z. Yang, J. Dong, W. Yang, Q.Y. An, L.Q. Mai, Electronic structure modulation in MoO<sub>2</sub>/MoP heterostructure to induce fast electronic/ionic diffusion kinetics for lithium storage, *Adv. Sci.* 9 (2022), 2104504, <https://doi.org/10.1002/advs.202104504>.

[61] S.S. Xu, X. Gao, A. Deshmukh, J.S. Zhou, N. Chen, W.F. Peng, Y.T. Gong, Z.Q. Yao, K.D. Finkelstein, B. Wan, F.M. Gao, M.Z. Wang, M.Y. Chen, H.Y. Gou, Pressure-promoted irregular CoMoP<sub>2</sub> nanoparticles activated by surface reconstruction for oxygen evolution reaction electrocatalysts, *J. Mater. Chem. A* 8 (2020) 2001–2007, <https://doi.org/10.1039/c9ta11775j>.

[62] H. Liao, X. Zhang, S. Niu, P. Tan, K. Chen, Y. Liu, G. Wang, M. Liu, J. Pan, Dynamic dissolution and re-adsorption of molybdate ion in iron incorporated nickel-molybdenum oxyhydroxide for promoting oxygen evolution reaction, *Appl. Catal. B Environ.* 307 (2022), 121150, <https://doi.org/10.1016/j.apcatb.2022.121150>.

[63] Y. Zhang, H. Guo, P. Yuan, K. Pang, B. Cao, X. Wu, L. Zheng, R. Song, Structural evolution of CoMoO<sub>4</sub> to CoOOH by ion electrochemical etching for boosting oxygen evolution reaction, *J. Power Sources* 442 (2019), 227252, <https://doi.org/10.1016/j.jpowsour.2019.227252>.

[64] Y. Li, Y. Wu, H. Hao, M. Yuan, Z. Lv, L. Xu, B. Wei, *In situ* unraveling surface reconstruction of Ni<sub>5</sub>P<sub>4</sub>@FeP nanosheet array for superior alkaline oxygen evolution reaction, *Appl. Catal. B Environ.* 305 (2022), 121033, <https://doi.org/10.1016/j.apcatb.2021.121033>.

[65] D.B. Jiang, Q. Zhang, L. Yang, Y.E. Deng, B. Yang, Y.C. Liu, C. Zhang, Z.H. Fu, Regulating effects of anthraquinone substituents and additives in photo-catalytic oxygenation of *p*-xylene by molecular oxygen under visible light irradiation, *Renew. Energy* 174 (2021) 928–938, <https://doi.org/10.1016/j.renene.2021.04.100>.

[66] K.C. Hwang, A. Sagadevan, P. Kundu, The sustainable room temperature conversion of *p*-xylene to terephthalic acid using ozone and UV irradiation, *Green Chem.* 21 (2019) 6082–6088, <https://doi.org/10.1039/c9gc02095k>.